



Photoacoustic computed tomography of mechanical HIFU-induced vascular injury

TRI VU,¹  YUQI TANG,¹ MUCONG LI,¹ GEORGII SANKIN,²
SHANSHAN TANG,³ SHIGAO CHEN,³ PEI ZHONG,² AND JUNJIE
YAO^{1,*}

¹Department of Biomedical Engineering, Duke University, Durham, NC 27708, USA

²Department of Mechanical Engineering and Materials Science, Duke University, Durham, NC 27708, USA

³Department of Radiology, Mayo Clinic College of Medicine, Rochester, MN 55905, USA

*junjie.yao@duke.edu

Abstract: Mechanical high-intensity focused ultrasound (HIFU) has been used for cancer treatment and drug delivery. Existing monitoring methods for mechanical HIFU therapies such as MRI and ultrasound imaging often suffer from high cost, poor spatial-temporal resolution, and/or low sensitivity to tissue's hemodynamic changes. Evaluating vascular injury during mechanical HIFU treatment, therefore, remains challenging. Photoacoustic computed tomography (PACT) is a promising tool to meet this need. Intrinsically sensitive to optical absorption, PACT provides high-resolution imaging of blood vessels using hemoglobin as the endogenous contrast. In this study, we have developed an integrated HIFU-PACT system for detecting vascular rupture in mechanical HIFU treatment. We have demonstrated singular value decomposition for enhancing hemorrhage detection. We have validated the HIFU-PACT performance on phantoms and *in vivo* animal tumor models. We expect that PACT-HIFU will find practical applications in oncology research using small animal models.

© 2021 Optical Society of America under the terms of the [OSA Open Access Publishing Agreement](#)

1. Introduction

High-intensity-focused-ultrasound (HIFU) has been explored over the past decade as an effective tool for cancer treatment [1]. In HIFU therapy, high-intensity acoustic waves are tightly focused at a targeted region of the tumor, resulting in either thermal or mechanical effects that may kill the tumor cells. With a high duty cycle, thermal HIFU relies on the absorption of acoustic energy, which results in high temperature rise [2] and tumor ablation [3–8]. With a low duty cycle, mechanical HIFU relies on pressure-induced acoustic cavitation, which can result in long-term anti-cancer immune response through cavitation-induced mechanical lysis and endogenous danger signals [9,10]. Mechanical HIFU can also be used for hemorrhage control [11], in which cavitation-induced platelet activation facilitates blood coagulation [11,12]. It has been shown that mechanical HIFU is advantageous over thermal HIFU in achieving systemic and long-lasting anti-tumor effect [13].

Despite its high potential, mechanical HIFU treatment still lacks an effective imaging tool for monitoring its hemodynamic impact, especially for identifying vascular rupture (*i.e.*, hemorrhage) [11]. Most reported methods, such as X-ray CT, magnetic resonance (MRI) and ultrasound (US) imaging, have focused only on monitoring the temperature rise during thermal HIFU treatment, but not on the mechanical HIFU-induced vascular damage [14,15]. MRI and X-ray CT have deep penetration depth and high temperature sensitivity [16,17], but suffer from low temporal resolution and high cost. US imaging, on the other hand, has both high frame rate and low cost. It can also detect the HIFU-induced cavitation signals, by actively imaging the cavitation bubbles (active cavitation mapping, ACM) or passively listening to the bubble collapsing (passive cavitation mapping, PCM) [18–22]. Nonetheless, US-based methods are not sensitive to static hemorrhage and slow blood flow [23,24].

Physically combining optical excitation and acoustic detection, photoacoustic (PA) imaging (PAI) is a promising solution for monitoring mechanical HIFU therapy. In PAI, a short-pulsed laser is used to illuminate the tissue. Some photons are absorbed by biomolecules such as hemoglobin in red blood cells, which induces a transient temperature rise [25]. The subsequent thermos-elastic expansion generates ultrasonic waves, which are detected by an ultrasonic transducer or transducer array to form a tomographic image of the original optical energy deposition. PAI is intrinsically sensitive to optical absorption contrast, and can achieve high spatial resolution at depths beyond the optical diffusion limit (~ 1 mm in soft tissue). Photoacoustic computed tomography (PACT) is a major implementation of PAI that typically uses wide-field light illumination and parallel ultrasound detection by an ultrasound transducer array. Taking advantage of its inherent signal dependence on temperature, PACT has been used for relative or absolute temperature mapping in thermal HIFU treatments *in vivo* [26,27]. Thus, we expect that, using hemoglobin as endogenous contrast, PACT can be potentially applied for detecting vascular damage in mechanical HIFU.

In this study, we report the feasibility of tracking mechanical HIFU-induced vascular injuries using a compact HIFU-PACT system, which integrates a HIFU probe for treatment and a linear ultrasound transducer array for PACT. We demonstrated the use of singular value decomposition (SVD) to enhance the detection of hemorrhage. The mechanical HIFU-induced cavitation was also captured by ACM. The performance of the HIFU-PACT system was evaluated by both phantom and *in vivo* experiments. This study provides a potential solution for monitoring mechanical HIFU-induced tissue damage in immunotherapy of cancers on small animal models.

2. Methods

2.1. Integrated HIFU-PACT system

The schematic of our HIFU-PACT system is shown in Fig. 1. For optical excitation, we used an Nd:YAG laser (Q-smart 850, Quantel) at 532-nm, with a 10-Hz repetition rate, a pulse energy of 98 mJ, and a beam diameter of 10 mm on the sample surface (Fig. 1(a)). The optical fluence on the sample surface was ~ 125 mJ/cm². Although the optical fluence on the sample surface is higher than the ANSI safety limit [28], we did not observe any laser-induced tissue damage. To detect PA signals, we used a 128-element L7-4 linear-array transducer, with a 5-MHz center frequency and a 50% bandwidth. The PA data acquisition was performed by using a commercial programmable US scanner (Vantage 128, Verasonics). The HIFU probe (H-102, Sonic Concepts) has a diameter of 64 mm, a focal length of 63.2 mm, a depth of focus of 10 mm, and a central frequency of 1.1 MHz. It has a central aperture (20 mm in diameter), allowing the pass of pulsed laser light (Fig. 1(a)). The system synchronization is shown in Fig. 1(c). An FPGA module (myRIO 1900, National Instrument) sent out flash lamp triggers to the pulsed laser with a 10 Hz repetition rate. After a Q-switch delay of $t_1 = 384$ μ s, a laser pulse was fired and the Verasonics scanner started recording the PA signals. After a delay of $t_2 = 30$ ms to prevent acoustic interference, the HIFU probe was triggered to transmit a train of sinusoidal waves. To drive the HIFU probe, we used 1.1-MHz sine waves (FG_{out}) with an amplified peak-to-peak amplitude of 60 V and a duty cycle of 30%. A lab-made voltage filter made of two parallel diodes was used to reject driving signals below 0.7 V when the HIFU probe was not transmitting. The 1.1-MHz sine waves passed through an impedance matching circuit and eventually drove the HIFU probe (Fig. 1(c)). We estimated that the peak negative pressure at the HIFU focus was ~ 12 MPa [29].

Each experiment session lasts for 50 seconds. The HIFU probe was turned on from 10 seconds to 40 seconds. The first and last 10 seconds provided pre- and post-treatment baseline. Before each experiment, we used B-mode US imaging to precisely position the target at the HIFU focus and inside the imaging plane of the PACT. The acquired raw PA signals were first bandpass filtered with cut-off frequencies of 4 and 7 MHz. PA images were reconstructed using the traditional delay-and-sum (DAS) method [30]. The spatial resolution achieved by the PACT

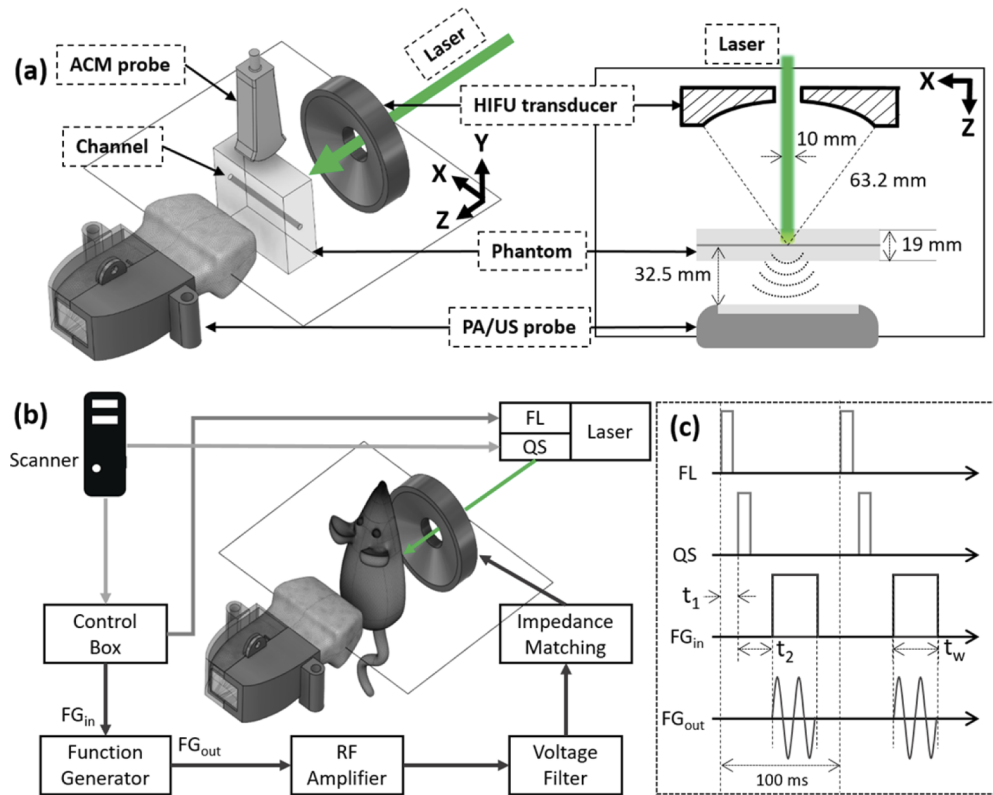


Fig. 1. Schematic of the integrated HIFU-PACT system. (a) Setup of the *in vitro* experiment, showing the channel phantom, HIFU probe, and PA/ACM transducers. (b) Setup of the *in vivo* experiment. (c) System synchronization. FL, flash lamp; QS, Q-switch; FG_{in}, trigger for HIFU transmission; FG_{out}, driving signal of the HIFU probe; t_1 , delay of the laser Q-switch; t_2 , delay of the HIFU transmission.

system is 400 μm along the lateral dimension, 425 μm along the axial dimension, and 1 mm along the elevational dimension [27]. In the phantom study, to capture the HIFU-induced cavitation activities, another micro-convex ultrasound probe (C15, SonoSite) and the scanner (180PLUS, SonoSite) were used for ACM (Fig. 1(a)). Similar to US B-mode imaging, in ACM, acoustic waves were transmitted and the echo signals reflected by the cavitation bubbles were detected. The ACM images provided the positions and shapes of the bubbles.

2.2. *In vitro* phantom experiment

For *in vitro* evaluation, we prepared a tissue-mimicking phantom made of 3% agar, which had similar acoustic cavitation behavior to soft tissues [22]. The agar phantom had a 1.2-mm diameter channel inside (Fig. 1(a)), mimicking a major blood vessel. During the experiment, a mixture of whole bovine blood and TiO₂ particles was pumped through the channel at a volume flow rate of 10 $\mu\text{L}/\text{min}$. TiO₂ particles were used as cavitation nuclei to facilitate bubble activity. The ACM probe was positioned above the phantom with its imaging plane intersecting the HIFU focus.

2.3. *In vivo* animal experiment

We next used the HIFU-PACT system to monitor the tissue damage during mechanical HIFU treatment of a mouse tumor model (Fig. 1(b)). We subcutaneously injected 4T1 breast cancer

cells in the upper leg of Balb/c mice. Mechanical HIFU was then performed when the tumor grew to ~6 mm in diameter. The animal protocol was approved by the Institutional Animal Care and Use Committee (IACUC) of Duke University. The HIFU focus was positioned at ~1 mm beneath the skin surface. The other HIFU settings were the same as the phantom experiment. For the *in vivo* experiment, we did not perform ACM due to the poor contrast of cavitation inside the tissue and also the difficulty of transducer alignment.

2.4. Motion correction

To better quantify hemodynamic change *in vivo*, we applied post-processing breathing motion correction to PA images, using phase-correlation based sub-pixel registration [31]. Briefly, the registration method uses the analytical solution of the phase correlation function for sub pixel shift between consecutive frames [31,32]. The sub-pixel displacements (Δx , Δz) along the lateral and axial direction are given by the main ($C(0, 0)$) and side peaks ($C(0, \pm 1)$ and $C(\pm 1, 0)$) of the inverse Fourier transform of the phase correlation [31,32]:

$$\Delta x = \frac{1}{2} \left(\frac{C(1, 0)}{C(1, 0) \pm C(0, 0)} + \frac{C(-1, 0)}{C(-1, 0) \pm C(0, 0)} \right) \quad (1)$$

$$\Delta z = \frac{1}{2} \left(\frac{C(0, 1)}{C(0, 1) \pm C(0, 0)} + \frac{C(0, -1)}{C(0, -1) \pm C(0, 0)} \right) \quad (2)$$

If necessary, additional manual image translation was performed on each PA image to further improve the motion correction. To quantify the area of PA-detected hemorrhage, the motion-corrected PA image was first binarized using the Otsu's method [33]. Next, in the region of interest, we counted the total number of effective pixels above the threshold weighted by the neighboring pixels at each point [34]. We used the Imaging Processing Toolbox of Matlab for the area quantification.

2.5. SVD filtering of HIFU-induced damage

As demonstrated by Zhang et al., spatiotemporal filtering can effectively enhance the signal-to-noise ratio (SNR) in PAT [35]. In our work, the spatiotemporal filtering was particularly useful for extracting the blood vessel ruptures and identifying the vascular injury during mechanical HIFU treatment. To better detect the HIFU-induced hemorrhage, we employed singular value decomposition (SVD) on the motion-corrected reconstructed PA images [35,36]. Singular value truncation was subsequently applied to remove the stationary PA signals from the blood vessels and highlight the signal changes from hemorrhage induced by the HIFU treatment [37,38]. Here, we selected an optimal cutoff singular value component (SVC) that maximally rejected the singular vectors corresponding to stationary blood signals as well as noises. We applied the SVD processing over every batch of 50 consecutive PA images acquired in 5 seconds.

The optimal cutoff SVC for each data was empirically searched within a range of 1 to 10 with a step size of 1. At each SVC step, a target-to-background ratio (TBR) was calculated between the in-focus (target) and out-of-focus (background) region after the SVD filtering. TBR was similar to SNR, in which the "signal" was the change in PA intensity of the target region, and the "noise" was the static PA intensity of the background region. The optimal cutoff SVC should maximize TBR. The TBR was computed as:

$$TBR = \frac{\mu_{target}}{\sigma_{background}} \quad (3)$$

in which, μ and σ are the mean and standard deviation of the PA signals in the region of interest. The target and background regions were marked by the blue and red box respectively in Figs. 3 and 5. From the TBR results in Fig. 2, we selected the optimal cutoff SVCs of 7 and 3 for

phantom (Fig. 3) and *in vivo* (Fig. 5) SVD filtering, respectively. In addition, we noticed that the *in vivo* data has overall lower TBR than the phantom data, mainly due to the remaining motion artifacts of the mouse.

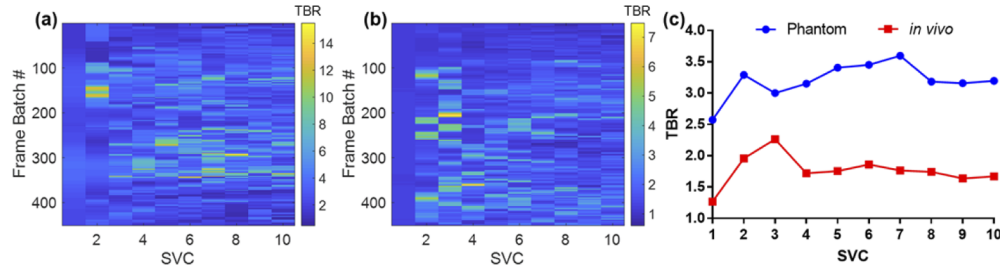


Fig. 2. Searching for the optimal cutoff SVC based on TBR. (a-b) Maps of TBR at different cutoff SVCs on the sliding 50-frame batch for phantom and *in vivo* data respectively. (c) Averaged TBR of all frames at each cutoff SVC.

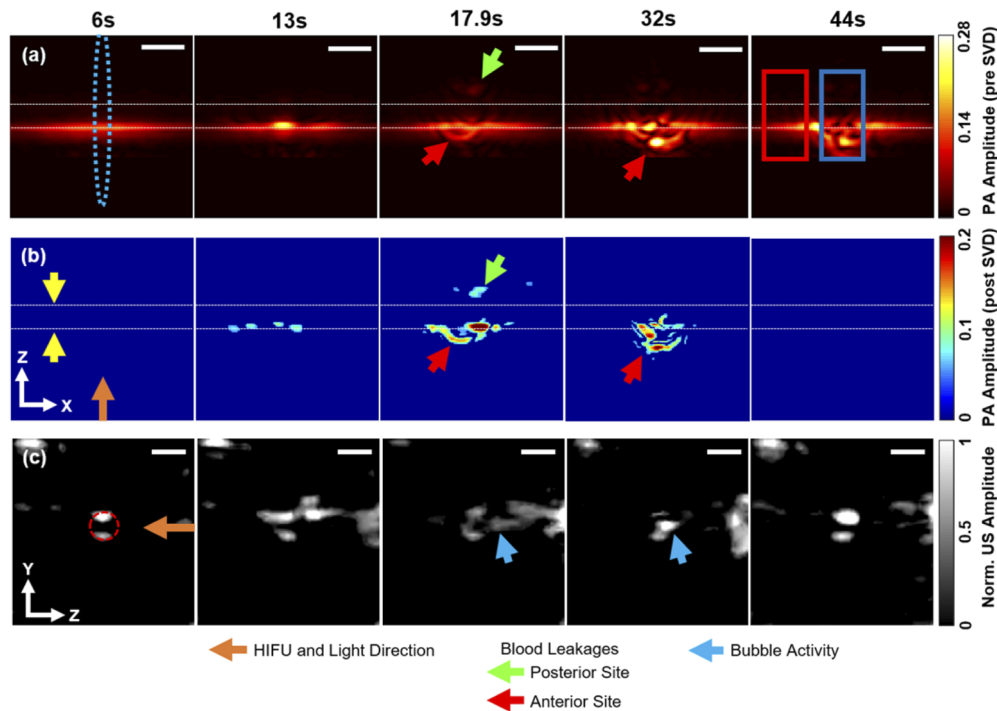


Fig. 3. PACT detection of HIFU-induced hemorrhage in a blood-channel phantom. (a) Pre-SVD and (b) post-SVD PA images at different timepoints, showing the enlarging PA signal areas (red and green arrows) as blood leaked from the channel (yellow arrow and dashed lines). The blue ellipse in (a) shows the HIFU focus. The blue and red boxes in and out of the HIFU focus were selected for further data analysis. (c) ACM detection of cavitation bubbles (blue arrows). The yellow arrows in (b) and red circle in (c) denote the position of the channel. Scale bar: 2 mm.

3. Results

3.1. In vitro phantom results

Figure 3(a) shows the reconstructed PA images of the blood channel at different time points, in which the blood leakage out of the channel was clearly observed. The excitation light was quickly attenuated inside the blood channel due to the strong optical absorption. Therefore, the front (anterior) portion of the channel was better imaged. The area of blood leakage within the HIFU focus was captured by PACT, as shown in Fig. 3(a) and Visualization 1. The nearly two-fold increase in PA signal area from 1.6 mm^2 to 3 mm^2 in Fig. 4(a) clearly showed the expanding leakage as compared to the background region out of the HIFU focus. We did not observe PA signal area change in the background region. Because we were not quantifying the PA signal intensity but the number of effective pixels above the noise floor, the expansion of PA signal areas outside the blood channel was not impacted by the possible HIFU-induced temperature rise. For the phantom experiment, no motion correction was needed. The post-treatment photograph (Fig. 4(b)) of the channel confirmed two leakage regions (anterior and posterior site), consistent with the PA results.

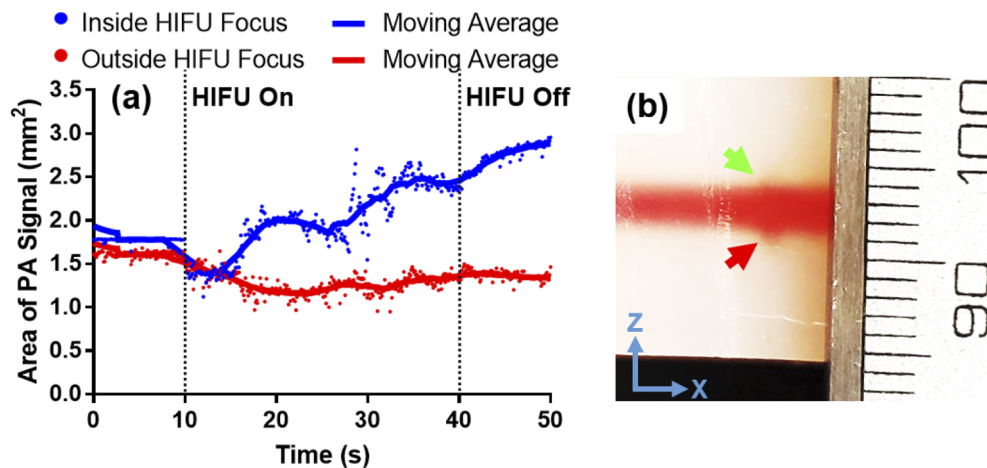


Fig. 4. Quantification of HIFU-induced hemorrhage in phantom. (a) The area of PA signal within the blue box (inside HIFU focus) and the red box (outside HIFU focus) in Fig. 3(a), respectively. The solid lines were smoothed over 50 data points. (b) Post-treatment photo of the vessel-mimicking channel, showing the larger blood leakage area in the front region of the HIFU focus (red arrow) than the back region (green arrow). The unit of the ruler is millimeter.

The blood leakage was due to the channel rupture as a result of the cavitation bubble collapse within the HIFU focus, as confirmed by the ACM results shown in Fig. 3(c). The ACM-detected cavitation activity also confirmed that the mechanical HIFU effect was the dominating factor in the channel rupture. At 1-second and 45-second when the HIFU transmission was turned off, no cavitation bubbles were detected by ACM, and no area change was recorded by PACT (Visualization 1). It is interesting to note that, the PACT results revealed that the channel rupture occurred mostly at the front side of the channel facing the HIFU transducer, which was consistent with previous studies [39,40]. This effect was mainly due to the scattering of the acoustic waves by the existing cavitation bubbles at the HIFU focus, which displaced the bubbles towards the HIFU transducer [25]. We would like to emphasize that the post-SVD results in Fig. 3(b) and Visualization 1 offered clearer depiction of the HIFU-induced PA signal change. Because the

stationary blood signals were suppressed, the SVD images showed only blood leakage and the damaged area during the HIFU treatment.

3.2. *In vivo* mouse tumor results

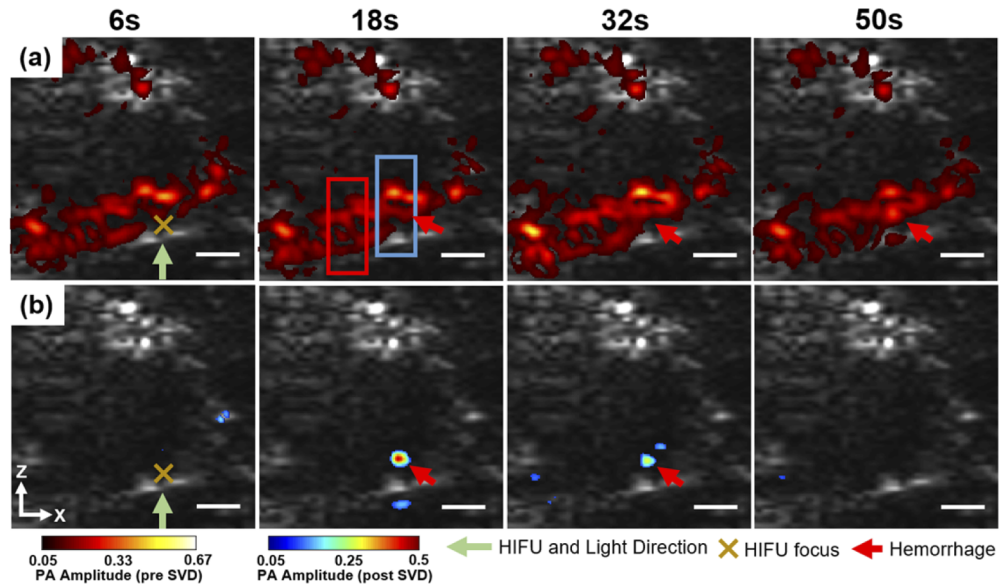


Fig. 5. PACT of *in vivo* vascular damage induced by mechanical HIFU. (a) Pre-SVD and (b) post-SVD PA images of the 4T1 tumor mouse model, overlaid on the B-mode US images at different timepoints during the HIFU treatment. The brown cross indicates the HIFU focus. The red arrows denote detected hemorrhage site during treatment. Scale bar: 2 mm.

The *in vivo* vascular damage detected by PACT was similar to the phantom experiment. During the HIFU treatment, there was a significant area expansion of the PA signals in the HIFU focus

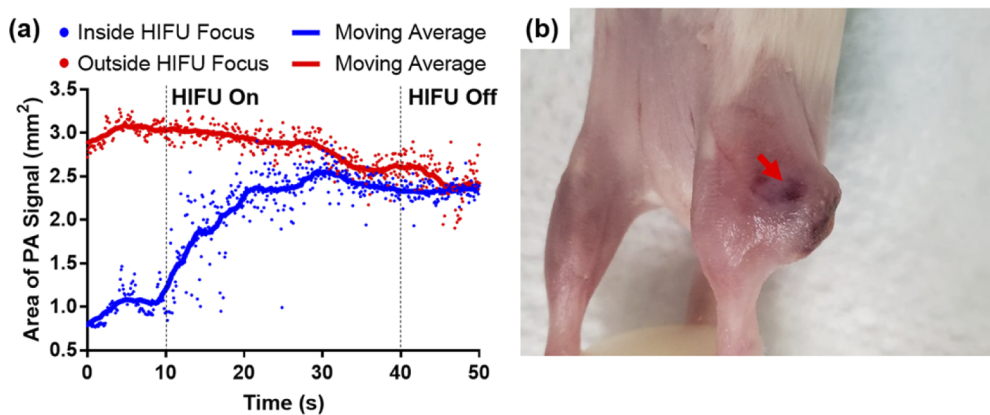


Fig. 6. Quantification of HIFU-induced hemorrhage in 4T1 tumor mouse model. (a) PA signal area within the blue box (inside HIFU focus) and the red box (outside HIFU focus) in Fig. 5(a). The solid lines were smoothed over 50 data points. (b) Post-treatment photo of the 4T1 tumor. The red arrow indicates the hemorrhage site.

from 1 mm² to 2.5 mm², indicating the onset of hemorrhage (Fig. 5(a) and Visualization 2). After suppressing the static signals from the surrounding blood vessels, the post-SVD images clearly revealed a major site of hemorrhage at the focal region (Fig. 5(b) and Visualization 2). The improved visualization by SVD is important for accurately identifying tissue injury in HIFU treatment. The PA signal area change shown in Fig. 6(a) was similar to the change in the phantom experiment, but there was a difference in the signal recovery. Towards the end of the HIFU treatment *in vivo* (after 30 seconds), the PA-detected hemorrhage area reached a plateau, probably due to the slow clearance of blood from the extravascular space. The PA-detected hemorrhage dynamic was consistent with the reported vascular injury by focused ultrasound treatment [41]. Post-treatment photograph validated the hemorrhage site beneath the skin (Fig. 6(b)).

4. Conclusion and discussion

In this study, we have developed an integrated HIFU-PACT system for inducing and detecting vascular injury during mechanical HIFU treatment. The phantom and *in vivo* experimental results have collectively demonstrated the feasibility of using PACT to monitor the vascular rupture with high resolution, deep penetration and high sensitivity. We have also demonstrated the application of the SVD filter to enhance the detection of HIFU-induced hemorrhage.

Currently, our system can provide only cross-sectional imaging of the HIFU focus, limited by the linear transducer array. Future work will focus on improving our HIFU-PACT system for 3D imaging with a high frame rate, by either incorporating elevational scanning or rotational scanning of the linear transducer array. Moreover, the quality of the *in vivo* PACT images of blood vessels is relatively poor, again because of the linear ultrasound array which is known to result in limited-view and limited-bandwidth artifacts for dense targets in photoacoustic imaging [42–45]. We will explore different image reconstruction and data processing methods to improve the image quality. For example, the 3D PA imaging quality can be improved by using a matrix transducer probe as well as model-based [46–49] or deep learning image reconstruction methods [50–52]. We have recently developed a reconstruction approach based on the Wasserstein Generative Adversarial Network with gradient penalty (WGAN-GP) to improve the image quality of PACT using a linear transducer array [53]. The *in vivo* fidelity of the WGAN-GP method needs further validation. In addition, the SVD filtering had to use 50 consecutive frames, reducing the effective processing speed. More work is needed to improve the efficiency of SVD filtering.

We can further combine the current setup with our recently-developed absolute temperature mapping method to compare the treatment effects of thermal HIFU and mechanical HIFU [27]. Moreover, previous studies have shown that vascular injury is closely associated with HIFU-induced immunotherapy by releasing tumor antigens. We will explore exogenous PA contrast agents that can target immune cells to simultaneously track the immune response, such as phytochrome-expressing T lymphocytes [54] and dendritic cells labelled by gold nanoparticles [55]. Ultimately, we expect that HIFU-PACT will provide valuable information on studying tissue's immediate and long-term responses during mechanical HIFU immunotherapy on small animal models.

Funding. National Institutes of Health (R01 EB028143, R01 NS111039, R21 EB027304, R21EB027981, R43 CA239830, R43 CA243822, R44 HL138185, RF1 NS115581); Duke Institute for Brain Sciences, Duke University (Incubator Award); American Heart Association (18CSA34080277); Chan Zuckerberg Initiative (2020-226178).

Disclosures. The authors declare no conflicts of interest.

Data availability. Data underlying the results presented in this paper are not publicly available at this time but may be obtained from the authors upon reasonable request.

References

1. E. Maloney and J. H. Hwang, "Emerging HIFU applications in cancer therapy," *Int. J. Hyperthermia* **31**(3), 302–309 (2015).

2. H. J. Jang, J.-Y. Lee, D.-H. Lee, W.-H. Kim, and J. H. Hwang, "Current and future clinical applications of high-intensity focused ultrasound (HIFU) for pancreatic cancer," *Gut and liver* **4**(Suppl.1), S57 (2010).
3. J. H. Hwang, Y.-N. Wang, C. Warren, M. P. Upton, F. Starr, Y. Zhou, and S. B. Mitchell, "Preclinical in vivo evaluation of an extracorporeal HIFU device for ablation of pancreatic tumors," *Ultrasound Med. Biol.* **35**(6), 967–975 (2009).
4. Y.-F. Zhou, "High intensity focused ultrasound in clinical tumor ablation," *WJCO* **2**(1), 8 (2011).
5. S. Y. Yeo, A. Elevelt, K. Donato, B. van Rietbergen, N. D. ter Hoeve, P. J. van Diest, and H. Gröll, "Bone metastasis treatment using magnetic resonance-guided high intensity focused ultrasound," *Bone* **81**, 513–523 (2015).
6. M. Huisman, M. K. Lam, L. W. Bartels, R. J. Nijenhuis, C. T. Moonen, F. M. Knuttel, H. M. Verkooijen, M. van Vulpen, and M. A. van den Bosch, "Feasibility of volumetric MRI-guided high intensity focused ultrasound (MR-HIFU) for painful bone metastases," *J. Ther. Ultrasound* **2**(1), 16 (2014).
7. H. Gröll and S. Langereis, "Hyperthermia-triggered drug delivery from temperature-sensitive liposomes using MRI-guided high intensity focused ultrasound," *J. Controlled Release* **161**(2), 317–327 (2012).
8. S. Dromi, V. Frenkel, A. Luk, B. Traugher, M. Angstadt, M. Bur, J. Poff, J. Xie, S. K. Libutti, and K. C. Li, "Pulsed-high intensity focused ultrasound and low temperature-sensitive liposomes for enhanced targeted drug delivery and antitumor effect," *Clin. Cancer Res.* **13**(9), 2722–2727 (2007).
9. Z. Hu, X. Y. Yang, Y. Liu, G. N. Sankin, E. C. Pua, M. A. Morse, H. K. Lyster, T. M. Clay, and P. Zhong, "Investigation of HIFU-induced anti-tumor immunity in a murine tumor model," *J. Transl. Med.* **5**(1), 34 (2007).
10. J. Unga and M. Hashida, "Ultrasound induced cancer immunotherapy," *Adv. Drug Delivery Rev.* **72**, 144–153 (2014).
11. S. Vaezy and V. Zderic, "Hemorrhage control using high intensity focused ultrasound," *Int. J. Hyperthermia* **23**(2), 203–211 (2007).
12. Z. Hu, X. Y. Yang, Y. Liu, M. A. Morse, H. K. Lyster, T. M. Clay, and P. Zhong, "Release of endogenous danger signals from HIFU-treated tumor cells and their stimulatory effects on APCs," *Biochem. Biophys. Res. Commun.* **335**(1), 124–131 (2005).
13. R. J. van den Bijgaart, D. C. Eikelenboom, M. Hoogenboom, J. J. Fütterer, M. H. den Brok, and G. J. Adema, "Thermal and mechanical high-intensity focused ultrasound: perspectives on tumor ablation, immune effects and combination strategies," *Cancer Immunol. Immunother.* **66**(2), 247–258 (2017).
14. B. D. de Senneville, C. Mougnot, B. Quesson, I. Dragonu, N. Grenier, and C. T. Moonen, "MR thermometry for monitoring tumor ablation," *Eur. Radiol.* **17**(9), 2401–2410 (2007).
15. C. J. Diederich, "Thermal ablation and high-temperature thermal therapy: overview of technology and clinical implementation," *Int. J. Hyperthermia* **21**(8), 745–753 (2005).
16. N. Weiss, J. Sosna, S. N. Goldberg, and H. Azhari, "Non-invasive temperature monitoring and hyperthermic injury onset detection using X-ray CT during HIFU thermal treatment in ex vivo fatty tissue," *Int. J. Hyperthermia* **30**(2), 119–125 (2014).
17. J. Wijlemans, L. Bartels, R. Deckers, M. Ries, W. T. M. Mali, C. Moonen, and M. Van Den Bosch, "Magnetic resonance-guided high-intensity focused ultrasound (MR-HIFU) ablation of liver tumours," *Cancer Imaging* **12**(2), 387–394 (2012).
18. C. R. Jensen, R. W. Ritchie, M. Gyöngy, J. R. Collin, T. Leslie, and C.-C. Coussios, "Spatiotemporal monitoring of high-intensity focused ultrasound therapy with passive acoustic mapping," *Radiology* **262**(1), 252–261 (2012).
19. B. A. Rabkin, V. Zderic, L. A. Crum, and S. Vaezy, "Biological and physical mechanisms of HIFU-induced hyperecho in ultrasound images," *Ultrasound Med. Biol.* **32**(11), 1721–1729 (2006).
20. B. A. Rabkin, V. Zderic, and S. Vaezy, "Hyperecho in ultrasound images of HIFU therapy: involvement of cavitation," *Ultrasound Med. Biol.* **31**(7), 947–956 (2005).
21. S. Vaezy, X. Shi, R. W. Martin, E. Chi, P. I. Nelson, M. R. Bailey, and L. A. Crum, "Real-time visualization of high-intensity focused ultrasound treatment using ultrasound imaging," *Ultrasound Med. Biol.* **27**(1), 33–42 (2001).
22. M. Gyöngy and C.-C. Coussios, "Passive spatial mapping of inertial cavitation during HIFU exposure," *IEEE Trans. Biomed. Eng.* **57**(1), 48–56 (2010).
23. T. Li, H. Chen, T. Khokhlova, Y.-N. Wang, W. Kreider, X. He, and J. H. Hwang, "Passive cavitation detection during pulsed HIFU exposures of ex vivo tissues and in vivo mouse pancreatic tumors," *Ultrasound Med. Biol.* **40**(7), 1523–1534 (2014).
24. S. D. Nandlall, E. Jackson, and C.-C. Coussios, "Real-time passive acoustic monitoring of HIFU-induced tissue damage," *Ultrasound Med. Biol.* **37**(6), 922–934 (2011).
25. L. V. Wang and J. Yao, "A practical guide to photoacoustic tomography in the life sciences," *Nat. Methods* **13**(8), 627–638 (2016).
26. Y. Zhou, E. Tang, J. W. Luo, and J. J. Yao, "Deep-tissue temperature mapping by multi-illumination photoacoustic tomography aided by a diffusion optical model: a numerical study," *J. Biomed. Opt.* **23**(01), 1 (2018).
27. Y. Zhou, M. Li, W. Liu, G. Sankin, J. Luo, P. Zhong, and J. Yao, "Thermal memory based photoacoustic imaging of temperature," *Optica* **6**(2), 198–205 (2019).
28. ANSI, "American National Standard for Safe Use of Lasers," (2014).
29. Y. Zhou, L. Zhai, R. Simmons, and P. Zhong, "Measurement of high intensity focused ultrasound fields by a fiber optic probe hydrophone," *J. Acoust. Soc. Am.* **120**(2), 676–685 (2006).
30. M. Xu and L. V. Wang, "Universal back-projection algorithm for photoacoustic computed tomography," *Phys. Rev. E* **71**(1), 016706 (2005).

31. H. Foroosh, J. B. Zerubia, and M. Berthod, "Extension of phase correlation to subpixel registration," *IEEE Trans. on Image Process.* **11**(3), 188–200 (2002).
32. P. Song, C. A. Cuellar, S. Tang, R. Islam, H. Wen, C. Huang, A. Manduca, J. D. Trzasko, B. E. Knudsen, and K. H. Lee, "Functional ultrasound imaging of spinal cord hemodynamic responses to epidural electrical stimulation: a feasibility study," *Front. Neurol.* **10**, 279 (2019).
33. N. Otsu, "A threshold selection method from gray-level histograms," *IEEE Trans. Syst., Man, Cybern.* **9**(1), 62–66 (1979).
34. W. K. Pratt, *Introduction to Digital Image Processing* (CRC Press, 2013).
35. G. Zhang, B. Wang, A. Stanzola, A. Shah, J. Bamber, and M.-X. Tang, "High signal-to-noise ratio contrast-enhanced photoacoustic imaging using acoustic sub-aperture processing and spatiotemporal filtering," in *2019 IEEE International Ultrasonics Symposium (IUS)(IEEE2019)*, pp. 494–497.
36. U.-W. Lok, P. Song, J. D. Trzasko, R. Daigle, E. A. Borisch, C. Huang, P. Gong, S. Tang, W. Ling, and S. Chen, "Real time SVD-based clutter filtering using randomized singular value decomposition and spatial downsampling for micro-vessel imaging on a Verasonics ultrasound system," *Ultrasonics* **107**, 106163 (2020).
37. X. Zhang, Z. Xu, N. Jia, W. Yang, Q. Feng, W. Chen, and Y. Feng, "Denoising of 3D magnetic resonance images by using higher-order singular value decomposition," *Med. Image Anal.* **19**(1), 75–86 (2015).
38. A. Rajwade, A. Rangarajan, and A. Banerjee, "Image denoising using the higher order singular value decomposition," *IEEE Trans. Pattern Anal. Mach. Intell.* **35**(4), 849–862 (2013).
39. J. Y. Siu, C. Liu, and Y. Zhou, "High-intensity focused ultrasound ablation around the tubing," *PLoS One* **12**(11), e0188206 (2017).
40. C. Coussios, C. Farny, G. Ter Haar, and R. Roy, "Role of acoustic cavitation in the delivery and monitoring of cancer treatment by high-intensity focused ultrasound (HIFU)," *Int. J. Hyperthermia* **23**(2), 105–120 (2007).
41. M. Li, B. Lan, G. Sankin, Y. Zhou, W. Liu, J. Xia, D. Wang, G. Trahey, P. Zhong, and J. Yao, "Simultaneous photoacoustic imaging and cavitation mapping in shockwave lithotripsy," *IEEE transactions on medical imaging* **39**(2), 468–477 (2020).
42. B. Huang, J. Xia, K. Maslov, and L. H. V. Wang, "Improving limited-view photoacoustic tomography with an acoustic reflector," *J. Biomed. Opt.* **18**(11), 110505 (2013).
43. Y. Xu, L. V. Wang, G. Ambartsoumian, and P. Kuchment, "Reconstructions in limited-view thermoacoustic tomography," *Med. Phys.* **31**(4), 724–733 (2004).
44. S. Preisser, N. L. Bush, A. G. Gertsch-Grover, S. Peeters, A. E. Bailey, J. C. Bamber, M. Frenz, and M. Jaeger, "Vessel orientation-dependent sensitivity of optoacoustic imaging using a linear array transducer," *J. Biomed. Opt.* **18**(02), 1 (2013).
45. S. B. Ma, S. H. Yang, and H. Guo, "Limited-view photoacoustic imaging based on linear-array detection and filtered mean-backprojection-iterative reconstruction," *J Appl Phys* **106**(12), 123104 (2009).
46. L. Ding, X. L. Dean-Ben, and D. Razansky, "Real-time model-based inversion in cross-sectional optoacoustic tomography," *IEEE Trans. Med. Imaging* **35**(8), 1883–1891 (2016).
47. L. Ding, D. Razansky, and X. L. Dean-Ben, "Model-based reconstruction of large three-dimensional optoacoustic datasets," *IEEE Trans Med Imaging* **39**(9), 2931–2940 (2020).
48. X. L. Dean-Ben, T. F. Fehm, S. J. Ford, S. Gottschalk, and D. Razansky, "Spiral volumetric optoacoustic tomography visualizes multi-scale dynamics in mice," *Light Sci Appl* **6**(4), e16247 (2017).
49. I. Ivankovic, X. L. Dean-Ben, H. A. Lin, Z. Zhang, B. Trautz, A. Petry, A. Gorch, and D. Razansky, "Volumetric optoacoustic tomography enables non-invasive in vivo characterization of impaired heart function in hypoxic conditions," *Sci. Rep.* **9**(1), 8369 (2019).
50. D. Allman, A. Reiter, and M. A. L. Bell, "Photoacoustic source detection and reflection artifact removal enabled by deep learning," *IEEE Trans. Med. Imaging* **37**(6), 1464–1477 (2018).
51. S. Gutta, V. S. Kadimesetty, S. K. Kalva, M. Pramanik, S. Ganapathy, and P. K. Yalavarthy, "Deep neural network-based bandwidth enhancement of photoacoustic data," *J. Biomed. Opt.* **22**(11), 1–7 (2017).
52. S. Guan, A. A. Khan, S. Sikdar, and P. V. Chitnis, "Fully Dense UNet for 2-D sparse photoacoustic tomography artifact removal," *IEEE J. Biomed. Health Inform.* **24**(2), 568–576 (2020).
53. T. Vu, M. Li, H. Humayun, Y. Zhou, and J. Yao, "A generative adversarial network for artifact removal in photoacoustic computed tomography with a linear-array transducer," *Exp. Biol. Med.* **245**(7), 597–605 (2020).
54. J. Yao, A. A. Kaberniuk, L. Li, D. M. Shcherbakova, R. Zhang, L. Wang, G. Li, V. V. Verkhusha, and L. V. Wang, "Multiscale photoacoustic tomography using reversibly switchable bacterial phytochrome as a near-infrared photochromic probe," *Nat. Methods* **13**(1), 67–73 (2016).
55. Y. J. Piao, H. S. Kim, and W. K. Moon, "Noninvasive photoacoustic imaging of dendritic cell stimulated with tumor cell-derived exosome," *Mol. Imaging Biol.* **22**(3), 612–622 (2020).